Combustion and Flame xxx (xxxx) xxx

Contents lists available at ScienceDirect

Combustion and Flame

journal homepage: www.sciencedirect.com/journal/combustion-and-flame

Laminar flame speed modification by Nanosecond Repetitively Pulsed Discharges, Part I: Numerical model

Colin A. Pavan *, Carmen Guerra-Garcia *

Massachusetts Institute of Technology, Department of Aeronautics and Astronautics, 77 Massachusetts Ave, Cambridge, 02141, MA, USA

ARTICLE INFO

Keywords:
Laminar flame speed
1D numerical model
Plasma-Assisted Combustion (PAC)
Nanosecond Repetitively Pulsed Discharges (NRPD)
Beneficial and adverse effects of plasma
Optimization of plasma actuation strategy

ABSTRACT

Plasma-assisted combustion (PAC) offers significant potential to enhance combustion processes by modifying thermal, kinetic, and transport properties. Despite progress in the field, challenges remain in reconciling disparate experimental results and understanding the mechanisms of plasma-flame interaction. This work develops a numerical modeling framework to systematically evaluate the impact of Nanosecond Repetitively Pulsed Discharges (NRPDs) on PAC systems. The focus of this contribution is modeling laminar premixed flames; and the main metric to assess the impact of plasma on flame is the laminar flame speed. The model is exercised on a stoichiometric methane/air flame. A combined 0D plasma-combustion model, *PlasmaChem*, is presented, enabling accurate energy tracking and coupling of detailed plasma and combustion mechanisms. The model is extended to 1D to incorporate compressible fluid dynamics, capturing the interaction between plasma and flame propagation. The results reveal distinct phases of plasma-flame interaction, demonstrating both beneficial effects, such as increased laminar flame speed due to radical production, and adverse effects, including flame deceleration from pressure disturbances. The model is compared to experiments in an accompanying paper, Part II of this work.

Novelty and significance

This work complements prior modeling studies that have included detailed 0D chemical kinetic models, phenomenological 3D models of plasma-assisted combustion, and self-consistent 1D and 2D simulations mostly devoted to ignition. In this work, we develop the first 1D flame model that integrates detailed plasma and combustion chemistry with compressible fluid dynamics, and allows for simulations over tens of milliseconds and parametric explorations. The model focuses on quantifying the impact of nanosecond repetitively pulsed discharges (NRPDs) on an important fundamental parameter, the laminar flame speed, unlike previous studies focusing exclusively on ignition delay time. The approach has revealed that the plasma can have both beneficial (increase) and adverse (decrease) effects on the laminar flame speed; reconciling discrepancies in the literature and offering a predictive tool to optimize PAC systems. The model is a step forward in enabling systematic parametric exploration, and facilitating rapid design iterations of plasma-assisted combustion phenomena.

1. Introduction

Plasma-assisted combustion (PAC) holds promise in enhancing combustion processes, but challenges persist in fully understanding its mechanisms and controlling the outcome of plasma actuation. Plasmas introduce several pathways for the modification of combustion, broadly grouped into three categories: (1) thermal effects, consisting of additional energy input that causes gas heating at various timescales, (2) kinetic effects, providing alternate reaction mechanisms through plasma-activated species and radicals, and (3) transport effects, caused by electric fields and other plasma forces acting on the fluid [1–3]. Determining the dominant mechanism in any given situation remains an open question and is often challenging to probe experimentally. Although there is a substantial body of literature on studying the impact of plasma on combustion behavior in various configurations [4–10], it is still difficult to compare between experimental arrangements and systematically assess the effects of plasma. For example, flame speed increases by plasma assistance in the range between 2-3% [11] and 100% [12] have been reported in the literature. Similarly, a wide range of values have been reported related to the extension in lean blowout limits [13]: with responses varying from a few percent, 5-10% [14–16], to a factor of above three in the limiting lean equivalence ratio [6].

* Corresponding authors.
E-mail addresses: cpavan@mit.edu (C.A. Pavan), guerrac@mit.edu (C. Guerra-Garcia).

https://doi.org/10.1016/j.combustflame.2025.114484
Received 15 March 2025; Received in revised form 28 August 2025; Accepted 13 September 2025

Numerical modeling tools can be used to reconcile the wide range of observations in the literature, in terms of plasma-enhancement on various combustion metrics; and to guide the design and optimization of plasma-assisted combustion systems. The complexity inherent in modeling the interaction between plasma and flame arises from the disparate timescales and lengthscales involved. The modeling landscape of plasma-assisted combustion (PAC) systems largely consists of three distinct categories. On one end are zero-dimensional kinetic models with detailed chemistry, such as those in Refs. [5,8,9]. While effective in capturing in detail the plasma-induced kinetic enhancements, these models overlook transport-driven processes. On the opposite end lie complex 3D reactive flow models, combined to simplified plasma models often referred to as *phenomenological models*, pioneered by Castela et al. [17–19]. These models are well-suited to address practical problems and simulate complex experiments: by reducing the plasma chemistry to the main species and thermal contributions, the models can track complex fluid interactions and simulate three-dimensional reactive flow environments. While extremely informative for the platform at hand, the results obtained from these complex systems are difficult to extrapolate to other environments. 1D and 2D models, that self-consistently solve for the electric field evolution by solving Poisson equation, are also common [20]. These models often solve for the initial phase of streamer propagation for ignition studies, and range from simulations that last a few nanoseconds to the hundreds of microseconds relevant for ignition.

This work aims to complement these modeling approaches by developing 1D models of PAC that preserve the fidelity of detailed plasma and combustion chemical kinetic mechanisms, while facilitating parametric exploration over extended timescales (a few tens of milliseconds), accounting for fluid dynamic effects, and focusing on combustion-enhancement metrics beyond the ignition delay time. In particular, the model developed in this work is that of a laminar premixed flame, which is used to explore the impact of nanosecond repetitively pulsed discharges (NRPD) on the laminar flame speed, S_L. By focusing on assessing the influence of plasma on fundamental combustion metrics, such as the laminar flame speed, it is possible to extract general recommendations and trends, and to explore the envelope of plasma-assisted enhancement. The chosen arrangement also offers practical utility in facilitating rapid design iterations and optimization of the plasma actuation strategy. The model allows for the systematic exploration of different actuation strategies (e.g. positioning and timing of the NRPD plasma relative to the flame front); as well as the detailed investigation of the relative contribution of the different mechanisms, including thermal, kinetic and transport effects, on the outcome observed.

The paper is divided as follows. Sections 2 and 3 discuss the development of a combined 0D plasma-combustion model, *PlasmaChem*, that leverages existing open-source tools. Similar models have been constructed by numerous groups, for example [9,21,22]. A focus of the model constructed here will be detailed energy tracking and conservation as data are passed between the tools; a topic that is not often discussed in similar works. Section 4 develops a 1D model of a laminar premixed unstrained flame, utilizing the 0D model as a building block. The model can solve both adiabatic flames and flames propagating in narrow channels. The model outputs, including the spatio-temporal evolution of the flame and the impact of NRPD on laminar flame speed, are demonstrated and briefly discussed in sections 5 and 6; with in-depth validation left to an accompanying paper, part II of this work, which compares the model to an experiment. Conclusions are summarized in Section 7.

2. PlasmaChem 0D model development

Combustion and plasma chemistry occur by different processes. Most elementary combustion chemistry reaction rates are primarily dependent on the gas temperature. This is true for the vast majority of the reactions contained in commonly used combustion chemistry models such as the GRI3.0 [23] and USC [24] mechanisms used for short-chain hydrocarbons. Plasma chemistry on the other hand is dominated by electron-impact reactions that do not depend on the gas temperature, but rather on electron temperatures. Accurate calculation of the reaction rates in non-equilibrium plasmas typically requires solving the Boltzmann equation so that the energy distribution of the electron population can be accounted for. This is particularly important when this distribution function is non-Maxwellian, as is typically the case for nanosecond repetitively pulsed discharges (NRPDs). In addition to requiring different methods of determining rate coefficients, the combustion and plasma chemistry can occur on vastly different time scales; this is especially true when the plasma is applied using the NRPD strategy that considers voltage pulses of nanosecond-timescale duration.

In light of these issues, it makes sense to model the plasma chemistry and combustion chemistry separately using optimized solvers for each to separate out the different processes and timescales. To this end, two existing open source tools were leveraged to handle the basic calculations for each process and a wrapper was built to handle passing of information between the two to couple them together in an efficient manner. The following sections describe these tools and their coupling. The 0D model was purposefully developed in such a way that an arbitrary combination of collision cross-sections, plasma-kinetic mechanism and combustion mechanism could be used.

The 0D model is written in the Julia language. Julia was chosen because it can run very quickly, at speeds comparable to compiled languages, with relatively simple syntax relative to other compiled languages. It also supports directly interfacing with compiled Fortran and C++ code, which was needed for utilizing the existing open source tools, and had good support on the available HPC cluster where the calculations presented in this work are run (the MIT supercloud [25]).

2.1. Subproblem solvers

The discharge kinetic sub-problem is solved using the open-source tool ZDPlasKin [26], a common choice amongst authors developing similar 0D PAC solvers [9,21]. This tool solves the zero-dimensional species conservation equations for an arbitrary plasma mechanism. It contains an integrated Boltzmann equation solver, BOLSIG+ [27], that allows reaction rate coefficients for electron impact reactions to be calculated during the transient evolution of the plasma at the instantaneous gas conditions. For use in the 0D solver, the Fortran-based ZDPlasKin code is compiled once for a given mechanism. The higher-level code, written in Julia, then directly interfaces with this compiled library by passing it the necessary parameters (species number densities, gas temperature, etc.).

Combustion kinetics and gas state properties are solved using the open source tool Cantera [28]. A Julia wrapper for Cantera is constructed similarly to as was done for ZDPlasKin. At the Julia level, a module was created to provide direct interface with several important features of Cantera: accessing (get/set) thermodynamic state properties (e.g. temperature, enthalpy, pressure), accessing (get only) derived/static thermodynamic properties (e.g. specific heat, molecular weight) and transport-driven properties (e.g. diffusion coefficients, thermal conductivity), accessing reaction rates and time-evolving reactors. Some of these functions, such as getting transport properties, are not utilized by the 0D model but are needed later for creating a 1D model.

The submodules were combined into a Julia module that contains access to all the lower-level functions and variables, along with a set of tools for 0D simulations. The layout of the 0D solver, as well as its extension to 1D, is shown in Fig. 1.

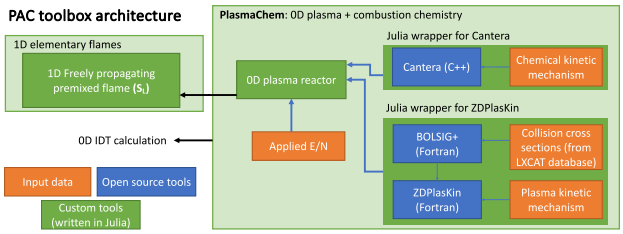

Fig. 1. Architecture of the PAC toolbox. The long timescale (many NRP pulses) 0D simulations are shown in Section 3, and 1D flame propagation is discussed in Section 4.

2.2. Separation of solution methods

2.2.1. Separation of time scales

In reality, the plasma and combustion chemical reactions occur simultaneously. The model, however, places the different mechanisms in different solvers and a technique for combining them is required. As there is a difference in time scales involved, it is useful to pick a technique that can solve each sub-problem with a different time step. The natural choice for this is an operator splitting scheme. This is a common technique for dealing with reacting flows and has previously been used in 0D PAC modeling by Refs. [21,29]. The theory is covered in many numerical methods texts (for example, see MacNamara and Strang [30]). The general procedure for the model in this work starts with Eq. (1), where f_c and f_p are the terms representing the combustion chemistry and plasma kinetics respectively, $\boldsymbol{\phi}$ is a vector of the system state (composition and temperature) and $\boldsymbol{\phi_0}$ is the initial condition (IC).

$$\frac{d\boldsymbol{\phi}}{dt} = f_c(t,\boldsymbol{\phi}) + f_p(t,\boldsymbol{\phi}) \quad \text{with IC } \boldsymbol{\phi}(t_0) = \phi_0 \tag{1}$$

Assume that, on short time scales, the functions f_c and f_p can be represented by linearized operators C and P acting on $\boldsymbol{\phi}$ and are time-independent.[1] Under these assumptions, it is possible to solve the equation for $\frac{d\boldsymbol{\phi}}{dt}$ on $[t_0, t_0+\Delta t]$ by solving two sub-problems sequentially, using the solution to the first as the initial condition for the second, as shown in Eq. (2).

$$\frac{d\boldsymbol{\phi}^*}{dt} = f_c(t,\boldsymbol{\phi}^*) \quad \text{with IC } \boldsymbol{\phi}^*(t_0) = \boldsymbol{\phi}_0 \tag{2a}$$

$$\frac{d\boldsymbol{\phi}}{dt} = f_p(t,\boldsymbol{\phi}) \quad \text{with IC } \boldsymbol{\phi}(t_0) = \boldsymbol{\phi}^*(t_0+\Delta t) \tag{2b}$$

In terms of accuracy, assuming that the linearized operators for the combustion and plasma chemistry do not commute and that the linearization approximation is valid, the method is first order accurate in time, with error scaling with $\mathcal{O}(\Delta t)$ [30]. Δt must be chosen relatively small; a value of 1 ns was found to be appropriate for simulating NRPDs (see [31]). In between discharge pulses, most of the plasma reactions are relatively slow and a much larger time step can be used. Typically, a value of 1 μs is used for 0D simulations. For 1D simulations, the fluid time-step is typically used. Note that these are the time steps used in the operator splitting scheme; each sub-problem solver (ZDPlasKin and Cantera) utilize several smaller sub-steps that are automatically chosen by the respective tools to ensure adequate convergence.

[1] It is noted by MacNamara and Strang [30] that stability and accuracy for non-linear operators is not gauranteed. Nevertheless, the method is still commonly used for non-linear reaction–diffusion equations.

2.2.2. Separation of species

There are three types of species that exist in the combustion and plasma kinetic mechanisms: (1) combustion-only species, (2) discharge-only species and (3) coupled species, which exist in both mechanisms. It is through this third type that the plasma is able to exert a kinetic effect on the flame. The combustion-only species consist primarily of minor combustion radicals and trace gases, which can be very important for the combustion chemistry but either do not exist in significant enough concentrations to need to be considered in the plasma mechanism, or have unknown behavior in the discharge. Examples include C2 and C3 hydrocarbons (when looking at methane combustion) and nitrogen compounds other than diatomic nitrogen. Discharge-only species are primarily short-lived excited states whose most important reactions occur with the coupled species, and ionized species/electrons. Examples include the electronically/vibrationally excited states of N_2 and ions of N_2, O_2 and CH_4. The coupled species are those that exist in highest concentration, and are therefore important to consider for electron-impact reactions, or the products of dissociative quenching, attachment and recombination, which are often important combustion radicals. Examples of the former include N_2, O_2 and CH_4, and of the latter O, H and CH_3.

Determination of the species that belong to each group is an automated process based on the provided input files. The program will automatically detect whether a particular species exists in just the combustion mechanism, just the discharge mechanism, or in both. To avoid reaction duplication, the plasma mechanism must only include reactions where at least one of the reactants or products is a discharge-only species.

During the operator splitting procedure, the number density of all species not included in the given submodule is held constant while the other submodule solves; e.g. the electron number density will not change while Cantera solves combustion kinetics. In order for this treatment to be valid, the mole fraction of discharge-only species must remain small. The combustion chemistry solver works with mole fractions, rather than number densities, and auto-normalizes mole fractions. Thus, in transferring species between the discharge and combustion solvers, a fractional error will be introduced on the order of the sum of the mole fractions of all discharge-only species. After solving the combustion problem, species mole fractions are converted back to number densities for communication with ZDPlasKin, taking into account the additional number density of species not tracked in the combustion solver. Provided the mole fraction of discharge-only species remains small, the error accumulated by this procedure in insignificant (<0.1% for all cases tested).

2.3. Energy conservation

By default, Cantera will solve the species evolution along with the energy conservation equation in 0D under either a constant volume or constant pressure assumption depending on user selection. In ZDPlasKin, the user can choose to turn the gas energy equation on or off. The form of the energy equation used by ZDPlasKin is given by Eq. (3), where $\dot{q}$ is the total energy source/sink from all reactions and heat input (in J $s^{-1}m^{-3}$), T_g is the gas temperature (in K), N is the total number density of heavy species (in part./m^3), and k_B is the Boltzmann constant (in SI units).

$$\frac{N k_B}{\gamma - 1}\frac{dT_g}{dt} = \dot{q} \tag{3}$$

This is equivalent to the constant-volume energy equation with the coefficient of the time derivative assumed to be constant. Thus, for consistency when using the operator splitting scheme, the solution in Cantera must be solved with a constant volume reactor assumption. This is reasonable as the timescale of an NRPD is much faster than the hydrodynamic expansion timescale and has important implications in the 1D model. The specific heat ratio (γ) used by ZDPlasKin is set

based on the value calculated by Cantera each time the solver switches between sub-models.

Cantera automatically calculates the internal energy of the mixture based on the state variables and the NASA polynomials [32]. Thus, energy is automatically conserved through all reactions, since the thermodynamic state properties in the combustion mechanism are all referenced to the same conditions. ZDPlasKin on the other hand does not automatically calculate the energy. $\dot{q}$ is composed of Joule heating, a user input source term, and the energy released or absorbed by all reactions. The first two terms are trivial to implement, and can generally be neglected for most problems considering NRPD. The energy released by reactions is more complicated since there is no automatic calculation of stored energy in ZDPlasKin. Proper treatment of the energy can be illustrated using an example.

Consider the two-step reaction shown below:

$$e + N_2 \rightarrow e + N_2(A^3, v = 0-4) \tag{4}$$

$$N_2(A^3, v = 0-4) + O_2 \rightarrow N_2 + 2O \tag{5}$$

The rate for the first reaction is determined by solving the Boltzmann equation, and the electrical energy required is automatically calculated based on the threshold energy value given in the cross-section file downloaded from LXCat [33]. From the SIGLO database [34], the threshold for this reaction is 6.17 eV, and so BOLSIG will calculate an input energy of 6.17 eV multiplied by the reaction rate. The second reaction has a rate given by reaction R100 in [35]. Since this is not an electron-impact reaction solved by BOLSIG, no energy is automatically calculated for it by ZDPlasKin. However, when species information is transferred to Cantera, the internal energy will increase by 5.166 eV for every O_2 molecule that has been dissociated due to the higher energy threshold of 2O relative to O_2, the reference state. Therefore, the energy contained in the dissociated products is implicitly accounted for when the state is set in Cantera. The difference in energy, 6.17 eV-5.166 eV=1.004 eV, has not yet been accounted for and so there will be a mismatch between the input energy calculated by BOLSIG and the change in total internal energy calculated by Cantera. An assumption is made that this additional 1.004 eV is released as heat to the gas. It is then handled by adding an energy release term of 1.004 eV to the second reaction, which will allow ZDPlasKin to account for this extra energy when it solves the energy equation. When the Cantera state is set, the temperature is now slightly higher and the change in internal energy will equal the amount of electrical energy input.

Correct energy tracking is also important in cases where mechanisms have been reduced. The species $N_2(A^3, v = 0-4)$ used in the previous example is not actually included in the plasma kinetic mechanism. Instead, the mechanism tracks a single species, $N_2(A)$, rather than each of its vibrational states independently. In the SIGLO database, there are three separate cross sections for $N_2(A^3)$ corresponding to vibrational states 0-4, 5-9 and 10+. In order to correctly account for energy input, a characteristic energy for the single $N_2(A)$ state tracked in the plasma kinetic mechanism had to be chosen. A value of 6.17 eV was chosen for this characteristic energy, corresponding to the threshold value listed in the database for vibrational states 0-4. All higher vibrational states were assumed to immediately quench to this state after being created, releasing the corresponding difference in energy as heat to the gas. For example, $N_2(A^3, v = 5-9)$ has an energy threshold of 7.00 eV. In the plasma kinetic mechanism, this reaction was written as $e + N_2 \xrightarrow{k_{5-9}} e + N_2(A) + 0.83$ eV where k_{5-9} is the reaction rate calculated by BOLSIG for the reaction $e + N_2(A^3, v = 5-9)$. This ensured all the input electrical energy was accounted for in the gas.

This procedure of quenching untracked species and releasing the difference in energy between them and the tracked species needs to be applied for all species that exist in the BOLSIG input file but not in the plasma kinetic mechanism in order to ensure correct energy conservation. One notable example of this is the vibrationally excited states of nitrogen. At moderate reduced electric fields in air (1-100Td), a significant amount of the input energy goes to vibrationally exciting nitrogen. Depending on the model, it may be unnecessary to track these states, particularly for 0D simulations that last much longer than the V-T relaxation time, but the energy input to these states and the heating it leads to needs to be accounted for. In these cases, the vibrationally excited states are instantly quenched according to Eq. (6), where k_v is the BOLSIG-calculated rate for the reaction $e + N_2(v = 0) \rightarrow e + N_2(v > 0)$ and $v \cdot 0.29$ eV is the energy contained in vibrational state v.

$$e + N_2 \xrightarrow{k_v} e + N_2 + v \cdot 0.29 \text{ eV} \tag{6}$$

Rotationally excited states are not explicitly quenched as doing this caused issues on inter-pulse timescales. Briefly, on inter-pulse timescales the electrons are assumed in thermal equilibrium with the background gas and have enough energy to excite rotational states; however, with no equation in the mechanism to transfer energy from the gas back to the electrons (as would be the case for true thermal equilibrium) this causes an artificial heating of the gas. The small amounts of energy going into rotational excitation (see Section 2.4.2) mean this has minimal impact on the results.

Explorations of energy deposition pathways and their relative importance are discussed in Section 3.2.

2.4. Model input selection

2.4.1. Combustion mechanism

This work considers stoichiometric methane/air premixed combustion. The combustion mechanism used for all simulations presented in this work is the GRI3.0 mechanism, which contains 53 species and 325 reactions [23]. Tests were additionally performed using the DRM19 mechanism, which is a reduced form of the GRI1.2 mechanism [36], and the USC-Mech Version II mechanism [24]. GRI3.0 balanced complexity, simulation run time and yielded flame speeds that closely match those measured in experiments (see example validation data provided with the mechanism [23]). This last point is especially important for this work as flame speed is a primary metric. However, the authors stress that the purpose of this work is to illustrate the modeling philosophy rather than rigorous comparison of different combustion mechanisms; changing mechanism is trivial within the current modeling framework.

2.4.2. Electron-impact reactions

All collision cross-sections were taken from the LXcat repository [33]. The species considered for electron impact reactions are N_2 with cross sections from the SIGLO database [34], O_2 with cross sections taken from the Phelps database [37], CH_4, H_2O, and CO_2, all with cross sections taken from the Hayashi database [38]. For this work, the interest is primarily in discharge acting on reactant gas that has not had a significant fraction of the fuel combusted. In this gas, the mole fractions of H_2O and CO_2 are relatively low and the discharge is governed by the premixed air-fuel mixture. It should be noted, however, that even low concentrations of water can have a notable impact on discharge behavior [39]. The energy deposition fraction, as a function of reduced electric field, for a stoichiometric methane-air mixture is shown in Fig. 2. As expected, N_2 vibrational states dominate at intermediate electric fields ($E/N < 100Td$) while electronic excitation dominates at higher fields ($E/N > 150Td$).

Given a profile for E/N, which is an input to the model, the electron multiplication ratio, $n_{e,r}$ can be calculated by Eq. (7), where k_{ion} is the effective mixture ionization rate, with units cm^3s^{-1}, and N is given in cm^{-3}.

$$n_{e,r} = \frac{n_e(t)}{n_{e,0}} = \exp\left(\int_0^t k_{ion}(t')N dt'\right) \tag{7}$$

To determine the relative rate of energy deposition over a single pulse, the energy deposition rates are weighted by the instantaneous electron density as shown by Eq. (8). k_A is the instantaneous energy

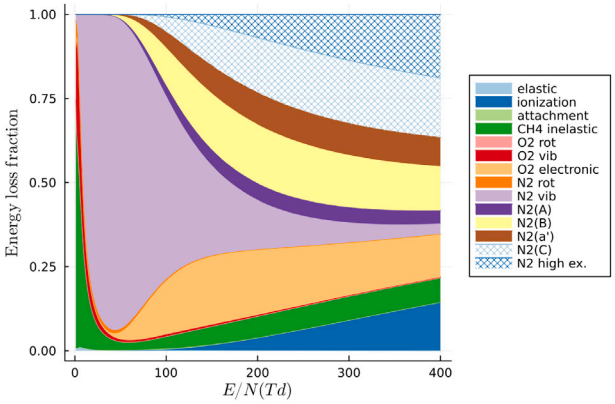

Fig. 2. Fractional energy deposition into different internal energy modes for stoichiometric methane-air, as a function of the reduced electric field. The area of each region at a given value of E/N represents the relative contribution of that loss mechanism; for example, at 300Td about 5% of the total input energy is consumed to produce N_2(A).

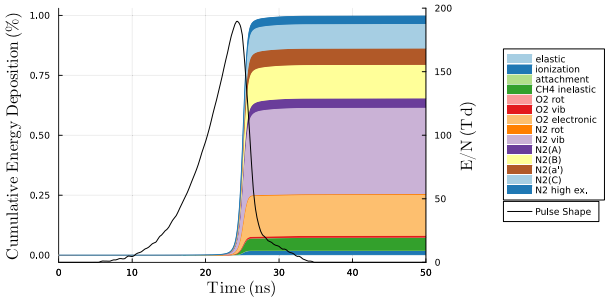

Fig. 3. Cumulative energy deposition fraction during pulse. The height of each region at 50 ns is the fraction of total pulse energy deposited by that mechanism. Pulse has a peak E/N of 190Td.

deposition rate through mechanism A with units $\mathrm{eVcm^{-3}s^{-1}}$ and w_A is the cumulative volumetric energy deposited by mechanism A with units $\mathrm{eVcm^{-3}}$.

$$\frac{w_A(t)}{n_{e,0}} = \int_0^t k_A(t')N n_{e,r}(t')dt' \tag{8}$$

Normalizing the volumetric energy by the total input energy during a pulse, $w_{tot} = \Sigma w_i$, the fractional energy deposited into the different mechanisms during a single pulse can be visualized. This is shown in Fig. 3. For the chosen cross-sections and pulse shape, in stoichiometric methane-air, roughly 38% of the input energy goes to electronically exciting N_2, 36% goes to vibrationally exciting N_2, 17% goes to electronically exciting O_2, 6% goes into all inelastic collisions with CH_4, 2% goes into ionization and the remaining 1% goes into all other mechanisms. These numbers generally agree with other works [40]; for example Castella et al. [17] assume about 45% of energy goes to vibrational excitation of nitrogen and 55% goes to fast gas heating and dissociation (which are both caused by electronic excitation of O_2 and N_2). Validation of the energy tracking scheme for our 0D model in a methane/air mixture is presented in [41].

Calculating E/N by the voltage divided by the gap distance for a given setup is not valid, since shielding effects will reduce the peak value and pulse duration. Simulations of NRP discharges in Dielectric Barrier Discharge (DBD) configurations such as [42,43] and experiments using the EFISH technique for insitu measurement [44] or other indirect methods [5,45,46] can give estimate of what shape and peak values should be expected. A NRP DBD discharge is chosen because that is the discharge used in the experiment of the accompanying paper, Part II of this work, and that the 1D model presented in Section 4 will seek to represent. The burner under study is a quartz channel, with the electrodes mounted on the dry side of the reactor (external surface, not in contact with the process gas, Fig. 7), so that the dielectric walls of the channel serve as the dielectric barriers of the DBD configuration (see Part II). The purpose of this work is not to self-consistently model the NRP DBD, so the pulse shape will be taken from the existing literature. A characteristic profile was chosen based on the simulated shape given in [42], scaled to have a peak value of 190Td. This peak value of the field was found to give a reasonable increase in electron number density each pulse, and is comparable to the peak value used by Lefkowitz et al. [47] in their similar modeling study. During the interpulse time, it is assumed that $T_e = T_{gas}$ and the electrons have a Maxwellian distribution. The total energy delivered by this pulse shape matches the order of magnitude observed in experiments [48], as will be seen in Part II.

2.4.3. Plasma kinetic mechanism

The plasma mechanism was initially based on the one given by Bak et al. [49], which is a relatively simple reaction scheme for a discharge in a methane-air mixture. Some changes were made to address shortcomings; for example, in the Bak mechanism there was only one slow recombination reaction for CH_4^+ and no charge exchange reactions. This resulted in a large population of CH_4^+ ions accumulating and not being effectively quenched, a problem that has been remedied in the improved mechanism.

The initial mechanism did not rigorously account for thermal energy input from the discharge, and so all reactions needed to have the energy release term added. The excited states produced by electron-impact reactions were assumed to have a stored energy equal to the threshold energy for the inelastic reaction. In cases where multiple species from the collision cross-section file were condensed into a single species, the procedure discussed in Section 2.3 was used. For dissociative quenching reactions, the stored energy of all involved particles was calculated and the difference in energy from the reactants and products sides was assumed to be heat released to the gas. For excited states of discharge-only species, including ions, the stored energy was the threshold energy for excitation. For coupled species, the stored energy in each species was calculated based on the total enthalpy at the reference temperature used by the NASA polynomials in the combustion mechanism (298.15 K), converted to a per-particle basis. This ensured consistency between ZDPlasKin and Cantera.

The final plasma kinetic mechanism used is included in ZDPlaskin input format in the supplementary material. It is also included in Appendix B to provide references for the various reactions. The purpose of this work was to use, rather than develop, the plasma kinetic mechanism. A known shortcoming of this mechanism is the simplified water chemistry. It is known that in humid air (including combustion products) H_3O^+ and its hydrates are some of the dominant species formed by charge exchange [39]. H_3O^+ is not included in the model, so recombination rates and recombination products may not be correct. However, the dominant impact of the plasma on combustion is through the excited states of N_2, and the electron impact dissociation of O_2 and CH_4, which are included so the mechanism should be suitable for use in an engineering model. A commonly used method of tracking vibrational energy is to use a vibrational temperature [17]. In contrast to this, the model used here explicitly models the first 8 vibrational states of $N_2(X)$ as these were available in the cross-section file. The de-excitation of these states is assumed to occur stepwise according to Eq. (9), where A is the particle on which $N_2(v > 0)$ quenches.

$$A + N_2(v) \xrightarrow{k_{v,v-1}} A + N_2(v-1) + 0.29\ \mathrm{eV} \tag{9}$$

The rates $k_{1,0}$ for A=N_2, H_2O and O are taken from [50], for A=O_2 from [51] and for A=CH_4 from [52]. From [50] equation 7.5 on page 107, $k_{v,v-1} = k_{1,0}v$ for molecules with no anharmonicity which will be the assumed behavior of N_2 at $v \leq 8$.

3. 0D model output

All simulations shown in this section are carried out with the gas initialized as a stoichiometric methane-air mixture (CH_4:O_2:N_2=1:2:7.52) at 300K and 1atm.

3.1. Species evolution during a single pulse

Fig. 4 shows the evolution of several important species from all three classes (combustion only, plasma only and coupled) during a single pulse. The smooth curves demonstrate that information is being passed between the sub-programs correctly. During the pulse (up to 200 ns), the timestep for operator splitting was set at 1 ns. Details during the pulse are shown in Fig. 4(a) and the inter-pulse period is shown in Fig. 4(b). In the latter figure, the x-axis is plotted on a log-scale to show both the pulse behavior and the interpulse behavior. During the interpulse, an operator splitting time step of 1 μs is used, which explains the sharp corners in the curves for H and N_2(A). During the pulse, large amounts of excited nitrogen species are produced. These decay at a rate inversely related to their energy of excitation, with N_2(C) being the shortest lived and N_2(A) being the longest. Several radicals, notably O, H and CH_3 are produced during the pulse, primarily by dissociative quenching of the excited N_2 states and direct electron impact dissociation. The production of these radicals is mostly complete by the end of the pulse (around 100 ns). Over inter-pulse timescales, these species react to form CO, CO_2, OH and H_2O, all of which are produced in negligible quantities during the pulse but steadily increase over the inter-pulse timescale. The population of ions and electrons is roughly constant after the pulse, and only begins to noticeably decline after round 10 μs, with the exception of N_2^+, which is rapidly consumed via charge exchange reactions to produce other ionized species. At the end of the interpulse period, the electron density and O_2^+ density are nearly equal, indicating that in this mechanism most ionized species, other than CH_4^+, will eventually undergo charge exchange to produce O_2^+. O_2^+ is then consumed by various recombination reactions. Note that the longest-lived ion being O_2^+ is an artifact of the mechanism used, but this is not expected to significantly impact the results, as the ions are not directly contributing to the combustion chemistry and the focus is on flame speed modification. Fig. 4(b) also shows the temperature change in the gas. There is a sharp increase caused by the quenching of the electronically excited nitrogen, followed by a more gradual increase on interpulse timescales driven by reactions/quenching of longer lived species. The initial sharp rise has important implications in the 1D model as it results in pressure waves in the gas. As this is the first pulse in a train, the overall temperature rise is relatively small; once a quasi-steady state has been reached (see 3.2), the temperature rise per pulse is greater.

3.2. Multi-pulse evolution and validation of energy conservation

Fig. 5 shows the accumulated effect of 10 pulses. This case demonstrates the energy conservation in the model and the impact of tracking individual N_2 vibrational states. In the top left plot, the energy conservation is shown. The *input energy* is the electrical energy input as calculated by the BOLSIG submodule within ZDPlaskin. This input energy is tracked as it is distributed to three different pathways. The first pathway, labeled Δe in the figure, is the change in internal energy of the ground-state species. It is calculated automatically by Cantera and includes the effect of the gas heating up and the increase in internal energy caused by molecular dissociation. The second pathway is the energy stored in ionized species, labeled e_{ion}. This makes up a negligible fraction of the total energy. The third pathway is the energy stored in vibrationally excited nitrogen species, labeled e_{vib}. A sizeable fraction of the input energy, roughly 30%–40% by Fig. 3, is stored in vibrational modes during the pulse. Over the inter-pulse timescale, these states quench and the energy becomes translational, being counted in the internal energy of the combustion species (VT relaxation). As shown in the plot, the sum of these three energy storage mechanisms approximately equals the electrical energy input. The slight discrepancy may be due to numerical inaccuracy or input energy going to rotational states that are not explicitly quenched. Temporary storage of energy does occur in electronically excited states, but these quench so rapidly, transferring their energy to internal energy of the ground state species that on the timescale of many pulses they store negligible energy. The top right figure shows the evolution of the key combustion radicals and products. During each pulse, the mole fraction of radicals increases significantly, and these are then consumed during the interpulse period. The result is a cyclic trend of creation and consumption. The combustion products (CO_2 and H_2O) and more stable radicals (CO) continually increase over the course of the simulation. The bottom left plot shows the charged species that are tracked in the model. After an initial transient to build up a baseline population, the charged species also reach a cyclic quasi-steady state. During the pulse, the plasma density increases and then recombination occurs during the interpulse time. The bottom right plot shows the vibrational states of nitrogen that are tracked in the model. These two reach a quasi-steady cyclic state, although the decay rate is slower than for the radicals or charged species. This slow decay rate leads to the heat release from VT relaxation.

Once the quasi-steady state is reached, each pulse deposits approximately 650μJ/cm^3. This number agrees well with the value measured in experiments (see [48,53]).

3.3. Fraction of energy input as gas heating

One of the open questions in the PAC literature is the relative importance of the different mechanisms of plasma actuation; specifically the effect of thermal energy input as compared to the kinetic enhancement. Simulations are a useful tool for this, since the mechanisms can be turned on or off. In Fig. 6, the gas heating equation is turned off in the ZDPlasKin submodule. This means that the discharge has only a kinetic effect, and the increase in internal energy comes entirely from the increase in internal energy caused by plasma-facilitated reactions. In this figure, the change in species concentrations are nearly identical to Fig. 5, indicating that enhancement of the Arrhenius rate combustion reactions due to higher temperatures when the energy equation is on has a negligible effect under these conditions. From the top left figure, only about 32% of the total input energy is captured as stored internal energy. This agrees well with Castela et al.'s estimate of 35% of energy going to dissociation [17].

4. 1D model construction

4.1. Governing equations

The general form of the model is a standard convection–diffusion system with source terms described by Eq. (10):

$$\frac{\partial \boldsymbol{\phi}}{\partial t} + \frac{\partial}{\partial x}\left(u\boldsymbol{\phi} + \boldsymbol{D}\right) = \boldsymbol{S_f} + \boldsymbol{S_r} \tag{10}$$

Where ϕ, $\boldsymbol{D}$, $\boldsymbol{S_f}$ and $\boldsymbol{S_r}$ correspond to the state variable, diffusive flux, fluid source term and reaction source term respectively. For a system consisting of the mass, momentum, energy and species conservation equations, these terms are written as Eq. (11). An earlier version of the model was presented in [54].

$$\boldsymbol{\phi} = \begin{bmatrix} \rho \\ \rho u \\ \rho e \\ \rho \boldsymbol{Y} \end{bmatrix}, \quad \boldsymbol{D} = \begin{bmatrix} 0 \\ 0 \\ -\lambda \frac{\partial T}{\partial x} + \sum j_k h_k \\ \boldsymbol{j} \end{bmatrix}, \quad \boldsymbol{S_f} = \begin{bmatrix} 0 \\ -\frac{\partial P}{\partial x} \\ -P\frac{\partial u}{\partial x} - \dot{L} \\ 0 \end{bmatrix}, \quad \boldsymbol{S_r} = \begin{bmatrix} 0 \\ 0 \\ \dot{q}_{plas} \\ \dot{\boldsymbol{w}} \end{bmatrix} \tag{11}$$

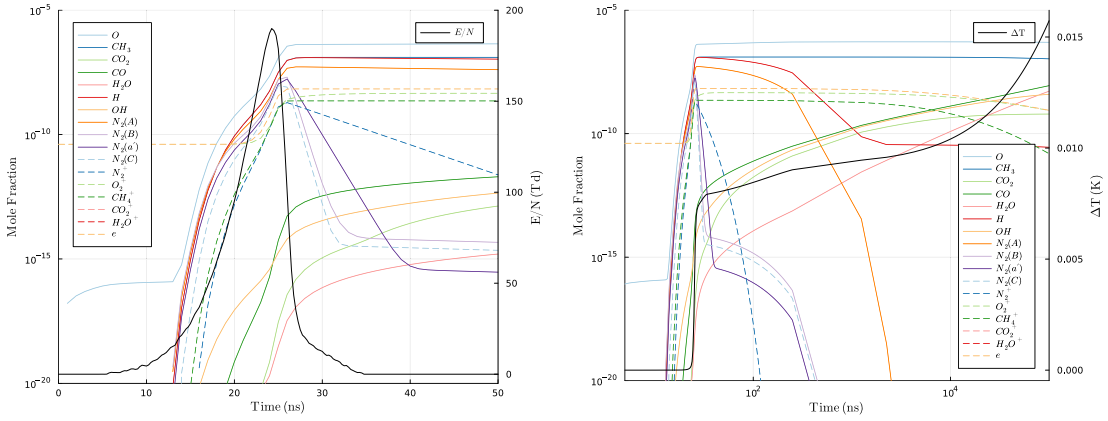

(a) Pulse only.

(b) Pulse plus interpulse period.

Fig. 4. Simulated species density evolution during a single pulse. An initial temperature of 300K and number density of $n_{e,0} = 10^9$ cm^{-3} was used. Left figure shows the pulse shape on the secondary axis, right figure shows the temperature evolution.

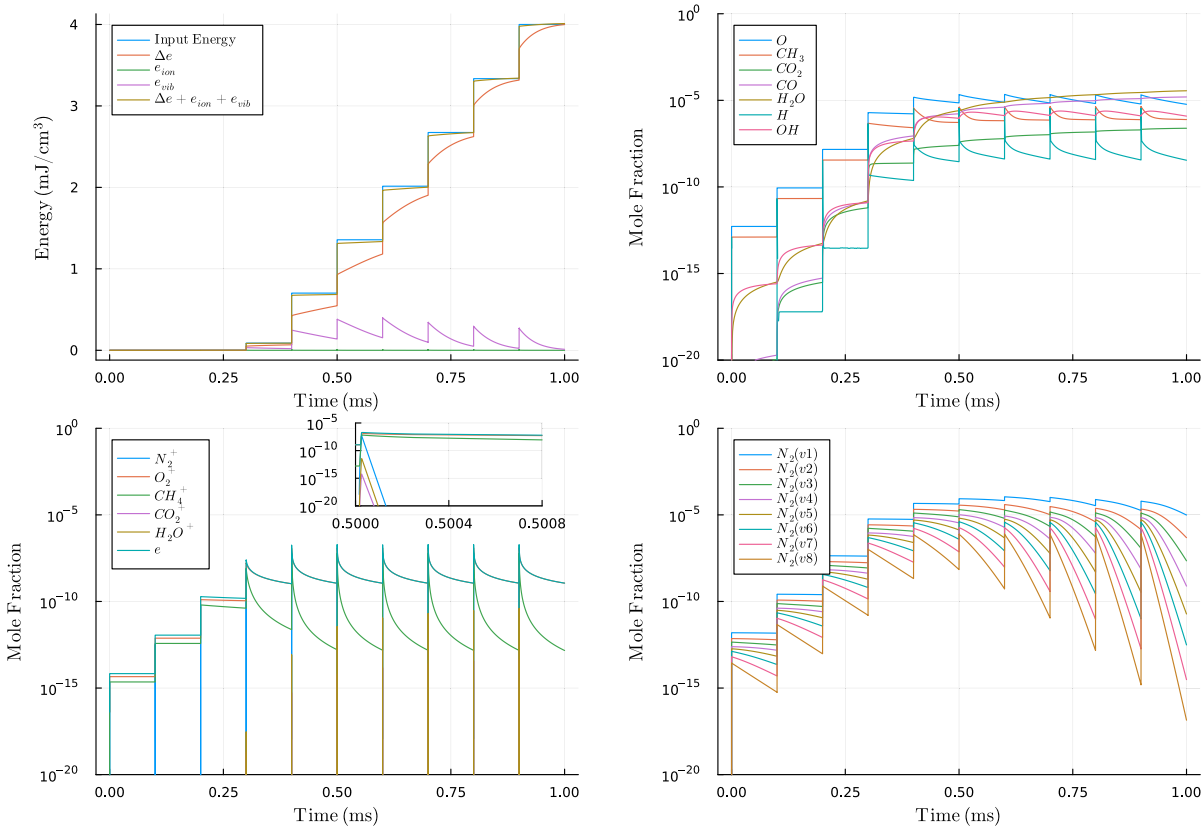

Fig. 5. Energy balance and species mole fractions during a 10 pulse simulation. The inset in the bottom left figure shows the first microsecond after the sixth pulse to illustrate the rapid decay of several plasma species.

Where ρ, u, e and $\boldsymbol{Y}$ are the tracked variables representing density, velocity, internal energy and mass fraction respectively. j_k is the diffusive mass flux of species k using the mixture averaged diffusion formulation, as in [28], λ is the thermal diffusivity, h_k is the enthalpy of species k and P is the pressure. The source terms $\dot{q}_{plas}$ and $\dot{\boldsymbol{w}}$ come from solving the combustion and discharge sub-problems in 0D, Section 2. $\dot{L}$ is the heat loss to the walls in a finite height channel. For the results presented in this paper, it is modeled assuming a rectangular cross-section channel of aspect ratio 8 with constant temperature walls at the unburned gas temperature, comparable to the experimental setup described in [48] and used for the experimental comparison in the accompanying paper, Part II. Table 8.1 in [55] gives a Nusselt number based on effective diameter of 5.60 in this case. The equation for $\dot{L}$ is then (12), where Nu is the Nusselt number and D_h is the effective hydraulic diameter (equal to 4 times the ratio of area to perimeter for a non-circular pipe).

$$\dot{L} = 4\lambda \frac{Nu}{D_h^2}(T - T_{\text{wall}}) \tag{12}$$

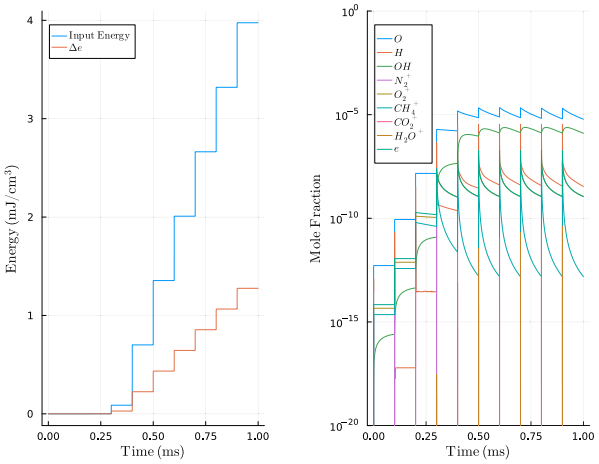

Fig. 6. Energy balance with gas heating equation turned off in ZDPlaskin.

To close the system, an equation of state is needed. Cantera is used for this as it will internally solve the relationship between internal energy, pressure and density. This is effectively the ideal gas law.

The system of equations can be written as Eq. (13), where subscripts f, c, p refer to the fluid, chemical and plasma sub-problems respectively.

$$\frac{\partial \boldsymbol{\phi}}{\partial t} = f_f(t, x, \boldsymbol{\phi}) + f_c(t, x, \boldsymbol{\phi}) + f_p(t, x, \boldsymbol{\phi}) \tag{13}$$

f_c and f_p are identical to the 0D model and have no impact on the momentum and mass conservation equations. f_f contains the convection, diffusion and fluid source terms. The same operator splitting method that was applied in the 0D model can be applied here, with an additional step to solve the fluid transport portion of the equation.

A common assumption when modeling 1D flames is to assume constant pressure. This is the strategy used by Cantera [28]. If pressure is constant, then the momentum equation becomes unnecessary. An initial version of the model used this assumption, but a problem was encountered when the discharge was applied. The discharge would cause rapid energy input under the electrode which would cause a decrease in density and an instantaneous increase in velocity throughout the domain to ensure mass conservation. In reality, this upset should be communicated via a pressure wave propagating at the gas sound speed. In order to capture these waves, a variable pressure is needed, hence the use of the compressible flow equations. All *discharge only* species, as defined in the 0D model, are assumed to be short lived and quench into *coupled* species on time scales of relevance to fluid transport. Therefore, to reduce the model complexity, these species are not considered in the transport model. They are assumed to be created only in cells in the discharge region and only participate in 0D reactions. This technique allows the model to handle detailed plasma chemistry without the system of transport equations becoming too large.

4.2. Simulation domain

The simulation domain is shown schematically in Fig. 7. It consists of a flame propagating in a rectangular cross-section channel of height h and width w. Note that these finite dimensions only impact the solution through determination of D_h in Eq. (12). For the results presented the width will be fixed at w =30 mm (as in prior experiments by the authors [48,53]) and the height h can be varied. Premixed methane and air enter upstream of the flame front flowing counter to the flame propagation direction. Unless otherwise noted, the unburnt mixture has an inlet flow speed of 5 cm/s in the lab frame and is initialized at 300K, 1atm and stoichiometric conditions (CH_4:O_2:N_2=1:2:7.52). A discharge is applied over a portion of the domain corresponding to the location of

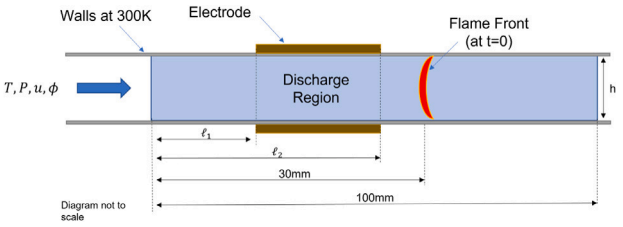

Fig. 7. Simulation domain for 1D model.

the electrode. This discharge is modeled as an NRP DBD using the same electric field as in the 0D model. All simulations begin by initializing the flame at x=30 mm. For the results presented in Part I, the electrode is positioned superimposed to the flame, a configuration referred to as the *in-situ* discharge configuration ($[\ell_1, \ell_2]$ = [25, 35] mm). This location and the electrode length are varied in Part II for a parametric exploration of actuation strategies. The simulation is 1D along the flame propagation direction, with the finite dimension of the channel taken into account by using an effective heat loss term that is proportional to the channel height and width by Eq. (12). For cases described as *infinite channel*, the heat loss term is set to zero, corresponding to the adiabatic flame condition in the absence of a discharge. The discharge is activated by applying the reduced electric field shown in Fig. 4.

4.3. Boundary conditions

As discussed above, the model needs to capture pressure waves that could be created by the discharge. When the discharge occurs in the unburnt gas, the reactive oxygen radicals will partially oxidize the fuel, causing rapid heat release and producing a pressure wave traveling at the speed of sound. This effect is exacerbated by fast gas heating effects from the plasma. Even though the total temperature increase from the discharge is only on the order of a few tens of degrees after several pulses, the rapid rate of energy input results in significant pressure perturbation, of the order of $10^0 - 10^1$ Pa, or a sound pressure level of around 100 dB. At the boundaries, a non-reflecting boundary condition, Eq. (14), is applied for $\psi \in [\rho, u, e]$ [56] where c is the local sound speed $c = \sqrt{\gamma RT}$.

$$\frac{\partial \psi}{\partial t} \pm c \frac{\partial \psi}{\partial x} = 0 \tag{14}$$

In Eq. (14), the positive sign corresponds to the wave traveling in the positive x direction (right boundary) and the negative sign corresponds to the wave traveling in the negative x direction (left boundary). This boundary condition is derived from the analytical solution of a wave propagating in an isentropic ideal gas; any source or diffusive terms in the vicinity of the boundary will invalidate the boundary condition. To address this, the simulation domain shown in Fig. 7 is extended with a region of frozen flow and no heat loss appended to both sides. In these regions, there are no gradients due to chemical reactions or thermal diffusion, ensuring that the conditions for the isentropic wave solution are met. If the simulation runs long enough that the small gradients that exist at x = 100 mm are advected to the downstream boundary, the simulation breaks because the gradient that Eq. (14) attempts to compensate for is not caused by an isentropic pressure wave. If this occurs, the domain must either be lengthened, or the solution re-started from a previous time step with the near-boundary conditions over-ridden to remove gradients in density and pressure.

4.4. Initial conditions

The 1D model initial condition is the steady state solution for flame propagation in a finite diameter channel without plasma. The steady

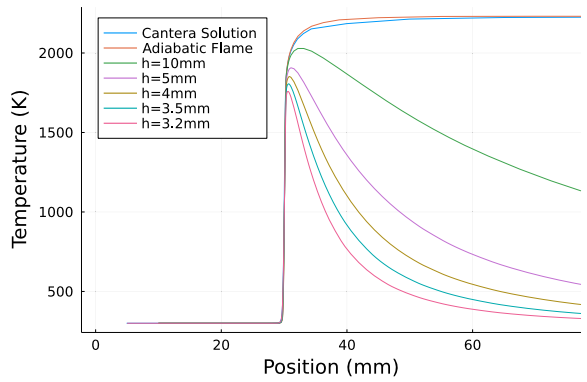

Fig. 8. Steady state solution for different channel sizes. The Cantera solution was used as the initial guess for the adiabatic flame and also for validation of the in-house solver.

state solution is found similar to [57], where the mass conservation equation is used as an eigenvalue equation for the velocity. The steady state solution for several different values of channel height are shown in Fig. 8. These are used as the initial conditions for the transient model with the corresponding channel. The plot also validates the solution obtained by the new solver, compared to the well-accepted Cantera solution.

4.5. Solution methods

The system is solved on a discretized grid with grid size chosen using an adaptive mesh refinement scheme. The default grid has $\Delta x = 5$ mm and this is selectively refined based on an error indicator. The error indicator is related to the local curvature of the solution; this work uses the form given in [58,59]. Spatial discretization of the differential equations is performed using a second order linear upwind difference scheme for the convection terms and a second order central difference scheme for the diffusion terms. Solutions to compressible flow equations on co-located grids for low Mach number flows are susceptible to a "checkerboard" instability. To handle this, a Rhie–Chow interpolation [60] method is used. The Rhie–Chow interpolation was performed using the methods outlined in [61,62]. An implicit time stepping scheme is used with a Jacobian that is constructed by taking advantage of the sparsity pattern of the problem. Jacobian construction is further optimized by using parallelism based on MPI. Further details on the solution optimization methods can be found in Ref. [31].

5. Model output

One case of the model output for demonstration purposes is shown here. Refer to the supplementary materials for animated versions of the model output. In the accompanying paper, part II of this work, the results of the model in different configurations are used to understand experimental results and explore both the beneficial effects of plasma (flame acceleration), and the adverse effects of plasma (flame deceleration). This is done by parametrically exploring the role of plasma positioning, relative to the flame front, as well as pulse repetition frequency.

5.1. Demonstration case

A demonstration of the model output is shown in Fig. 9. The example shown is for a channel of 3.5 mm height, with a pulse repetition frequency (PRF) of 8 kHz, a 10 mm-long electrode and the electrode positioned between ℓ_1 =25 mm and ℓ_2 =35 mm (see Fig. 7). The flame starting point is within the electrode region, therefore the plasma is deposited *in-situ* with the reaction zone of the flame. This corresponds to the same case presented in Part II of this work as 'strategy 3'.

The top left plot shows the instantaneous temperature profile at 4 ms increments and shows the flame advancing from right to left. The top center plot shows the flame speed relative to the incoming flow. The flame front location is defined to be the point where the density equals $0.6\mathrm{kg/m^3}$ and the flame speed is calculated based on the motion of this point relative to initial speed of the fresh gas (5 cm/s) prior to the discharge.[2] In this work, the flame front location is primarily used for calculation of flame speed and the fixed density value was used because it provided a simple method of identification. When the mesh is refined near the flame front, it can cause small jumps in the flame position, which is what is responsible for some of the spikes shown in the instantaneous speed. These do not affect the long term behavior as the offset forward/backward averages to zero over a full simulation, and can be partially removed from the results by sampling the position less frequently. The "Instantaneous" curve shows the flame speed by sampling the position every 2.5 μs, while the "Average" curve shows the speed when sampling every 125 μs. The average velocity calculation also removes the cyclic behavior caused by the pressure pulses and replaces them with an offset corresponding to the "average" effect the pressure waves have on the flame. In depth discussion of the effect of pressure waves is presented in part II of this work.

The right plot shows the instantaneous species mole fractions for several radicals and combustion products as a function of position at one point in time, when the flame front is located at approximately x=27 mm. Several regions can be identified. Far ahead of the electrode, there are negligible populations of all plotted species. Between about 20 mm and 25 mm, there is a transition region where radicals produced by the discharge have diffused and advected upstream of the flame. Between the left edge of the electrode (x=25 mm) and the flame front, there is a plateau in radical densities; the height of this plateau varies in time depending on the time since the last pulse and the total number of pulses, but the height is approximately uniform across the portion of the electrode that covers unburnt gas. At the flame front, there is a rapid increase in the density of all radicals, followed by a burnt gas region where combustion products have high mole fraction and intermediate radicals have decreased.

The final plot in the bottom left shows the instantaneous density of several radicals and ions at a fixed location 0.5 mm from the left edge of the electrode. There is a rapid increase during the first few pulses, followed by a period of periodic behavior. In this region, the species are produced during each discharge pulse and then are slowly consumed in between pulses before being regenerated on the next pulses. The consumption of radicals is in the form of both recombination reactions, and oxidative reactions with the fuel. The ions are consumed primarily by charge exchange and recombination. Once the flame passes x=25.5 mm, the production of radicals by the discharge is greatly decreased. There is still a high population of electrons and ionized oxygen, but at this point the temperature is high enough that the rate of O, OH and H atom production by thermal mechanisms is much higher than that produced by the discharge and the production of these species is no longer dominated by the discharge mechanisms.

Also shown in this plot is the average volumetric energy input from plasma (in black). This was calculated using the procedure described in Appendix A.

[2] While the gas starts by entering at the left edge of the domain at 5 cm/s, the non-reflecting boundaries mean that this value changes in time to compensate for pressure waves.

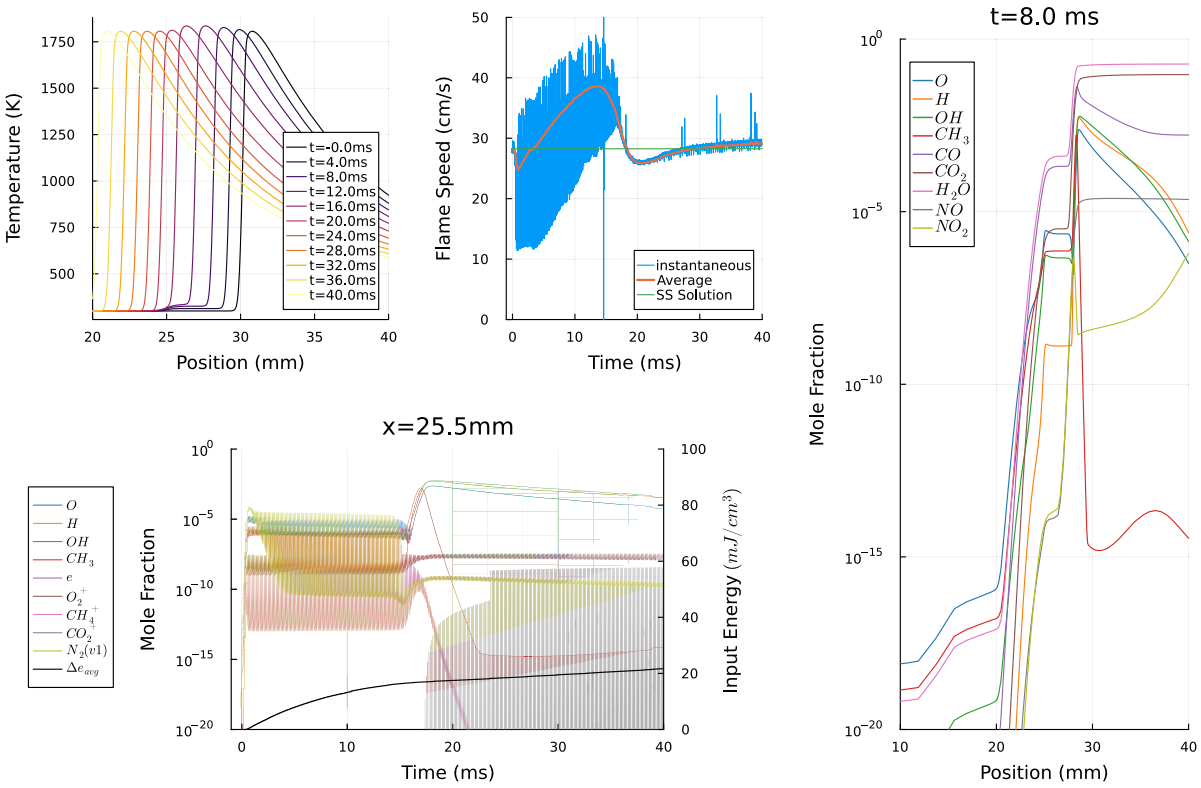

Fig. 9. Model outputs for the case with 8 kHz discharge applied in-situ with a flame in a 3.5 mm channel. Clockwise from top left: (1) temperature profile at various points in time, (2) flame speed measured relative to incoming gas, (3) spatially-resolved species mole fractions at t=8 ms, (4) time-resolved species mole fractions at x= 25.5 mm (0.5 mm from electrode left edge) and average volumetric energy input.

6. Discussion of model results

For comparison with experimental results and studying the macroscopic behavior of the flame acted on by plasma, the most important parameter is the flame speed (top center plot). The results shown in Fig. 9 show four distinct phases. When the discharge is turned on at time=0, there is a drop in the flame speed. This is caused by pressure fluctuations produced by the discharge. Much of the energy input from the plasma is rapidly converted to thermal energy by the sub-microsecond timescale quenching of the electronically excited nitrogen molecules. This rapid heat release produces a pressure wave traveling at the speed of sound which pushes against the flame front, causing it to slow down. In the second phase, a population of plasma-created radicals has built up ahead of the flame. These radicals, most notably atomic oxygen, participate in combustion reactions and result in an acceleration of the flame front. This is likely due to the background population of radicals within the convection–diffusion zone ahead of the flame being greater than the typical amount produced by dissociation due to the heat from the flame. Another contributor could be the higher gas temperature, as seen in the top left plot, although this is expected to be a less significant effect. In the third phase, the reaction zone of the flame reaches the edge of the electrode and no longer encounters a region of increased radical density. The flame rapidly slows down to a speed below the laminar flame speed. The cause of the undershoot is suspected to be that, because the flame was moving faster than normal, there was insufficient time for the heat to diffuse ahead of the flame and initiate reactions at the rate required to maintain the laminar flame speed. In the fourth and final stage, the flame speed returns to the baseline value in the absence of plasma perturbation.

A particularly interesting finding here is that the plasma has both a beneficial and adverse effect on the flame propagation depending one where it is applied. In the first stage, the adverse affect is due to fluid processes (the pressure wave). In the second stage, the beneficial effect is due to thermal and/or chemical processes (increased radical density and temperature). In the third phase, the adverse effect is related to the plasma upsetting the balance between propagation speed and diffusion timescale. All of these impacts have been observed in experiments, which is the subject of the accompanying paper, part II of this work. The model allows to gain physical insight from these experiments, as it allows for turning on and off mechanisms and isolating effects. It also provides far more information than the limited diagnostics of the experiment (fast imaging and electrical signals).

While the results presented here are expected to be qualitatively valid (a proposition that will be demonstrated in part II), it is important to note that quantitative predictions will be dependent on mechanism choice. The model developed here has intentionally been produced to allow combustion and kinetic mechanisms to be used interchangeably so that the most appropriate combination for any given scenario can be chosen. The plasma mechanism used was primarily built for species in the unburned mixture and likely is not the optimal choice for discharges in the burned gas. Nevertheless, important insights have been obtained, and the model has made a number of novel, testable predictions.

7. Conclusion

This work presented the development of two models for NRP plasma based PAC systems. The first is a 0D model built on top of existing open source tools. The second extends the 0D model to one dimension in cartesian coordinates to represent a laminar premixed flame (unstrained flame). Both tools are capable of simulating the accumulated effect of many NRP pulses with detailed combustion and plasma chemistry, with the 1D model also including the effects of fluid dynamics. The model is well suited to being used for parametric exploration of different operating conditions, especially pulse repetition

frequency and electrode placement. The model was developed with a focus on ensuring accurate energy and species conservation between the different components, and on being made computationally efficient to make multiple simulations feasible.

The model provides useful insights into plasma assisted combustion. The detailed energy tracking enabled by the 0D PlasmaChem solver provides a flexible method of determining energy deposition pathways and separating thermal and kinetic effects. The 1D solver has demonstrated the importance of the location of the plasma actuation relative to the flame front as will be further explored in Part II of this paper. In particular the model can be used to explore the influence of NRP plasma on a key fundamental parameter: the laminar flame speed. This extends prior works that have focused on ignition delay time reduction exclusively. The sample results presented in this paper reveal that plasma has both an adverse effect, due to pressure wave disturbances triggered by the repetitive rapid energy deposition, as well as a beneficial effect, due to the kinetic and thermal enhancements by plasma. By using a numerical model, the benefits and detriments of the plasma can be systematically evaluated, as a function of pulse repetition frequency and electrode position. These findings may help explain the variable behaviors, and degrees of flame speed enhancement, observed in the literature for different experiments. Part II of this work will parametrically explore these variables and provide an experimental validation of the phenomena revealed by the numerical model.

CRediT authorship contribution statement

Colin A. Pavan: Writing – original draft, Visualization, Validation, Software, Methodology, Investigation, Formal analysis, Data curation. **Carmen Guerra-Garcia:** Writing – review & editing, Supervision, Resources, Project administration, Methodology, Funding acquisition, Conceptualization.

Declaration of competing interest

The authors declare that they have no known competing financial interests or personal relationships that could have appeared to influence the work reported in this paper.

Acknowledgments

This work has been supported by the Office of Naval Research (ONR), USA Award Number N00014-21-1-2571, and by the National Science Foundation (NSF), USA Award Number 2339518. C.P. was partially supported by a Mathworks Fellowship at the time the work was performed.

Appendix A. Energy conservation in 1D

From the 0D analysis, all the electrical energy input ultimately is transferred from the electrons to the gas. The energy input to the gas in the 1D model is calculated from a control volume analysis of the energy equation using Eq. (A.1). Diffusion losses across the boundaries are assumed negligible. The integration over x and t yields units of energy per unit area. The average volumetric energy deposited by the plasma, $\bar{w}_{pl}$ can be calculated by division by the electrode length ℓ as shown in Eq. (A.2).

$$\iint_{x,t} \dot{q}_{plas} = \iint_{x,t} \frac{\partial(\rho e)}{\partial t} - \iint_{x,t} \left[-\frac{\partial}{\partial x}(\rho u e) - \dot{L} - P\frac{\partial u}{\partial x} \right] \tag{A.1}$$

$$\bar{w}_{pl} \left[J/m^3 \right] = \frac{1}{\ell} \iint_{x,t} \dot{q}_{plas} \tag{A.2}$$

When the flame is far from the electrode, the energy input is approximately uniform across the full electrode, however once the flame enters the electrode region the deposition becomes highly non-uniform. Input power is proportional to $n_e \mu E^2 = N^2 n_e \mu \left(\frac{E}{N}\right)^2$, where

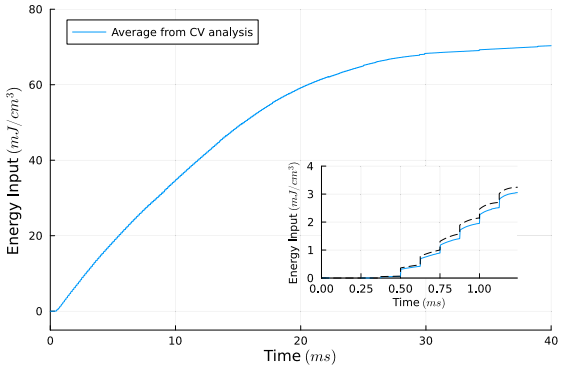

Fig. A.10. Comparison of model energy calculation using Eq. (A.2) ("Average from CV analysis") for a case where the discharge occurs ahead of the flame and the flame passes under the electrode. Inset shows the first 10 pulses as compared to the 0D model (black dashed line). (For interpretation of the references to color in this figure legend, the reader is referred to the web version of this article.)

μ is the electron mobility, and n_e the electron number density. For a fixed E/N profile as is used in these tests, and assuming that the energy deposition is dominated by collisions with nitrogen (a mostly inert species with approximately constant mole fraction), the input energy during a single pulse scales as $w_{pl} \propto N \int n_e dt$ since the product μN is constant for a given composition and E/N profile [27].

Fig. A.10 shows an example energy calculation by Eq. (A.2) for a case where the flame starts ahead of the electrode and then enters it. The inset shows the energy deposition for the first 10 pulses, when the condition under the electrode is uniform and there is no significant variation in energy input with x, compared to the solution from the 0D model run under the same conditions. Both are very similar, validating the energy measurement method. The deviation of the 1D energy calculations from the 0D energy calculation is about 10%, and be explained by errors in numerical integration/numerical solution of the ODEs and transport of energy outside of the electrode. The energy input is negligible for the first few pulses due to the low electron number density at the start; both simulations are initialized with $n_{e,0} = 10^3$ cm^{-3}. Then, the cumulative (average) energy input starts to increase linearly with number of pulses. As the gas under the electrode starts to heat and the number density drops, the curve develops slightly negative curvature. Once the flame reaches the edge of the electrode (around 12 ms), the region in the burned gas starts depositing significantly less energy and the average energy input becomes significantly less. Once the flame has fully passed the electrode and the discharge is purely in the burned gas, around 28 ms, the energy input is linear again but significantly less than before the flame reached the electrode.

Appendix B. Plasma mechanism

This appendix summarizes the plasma mechanism used in this work. The input file in ZD plaskin format is included in the supplementary material. Reactions in the plasma mechanism are grouped by type in Tables B.1–B.7. For electron impact reactions, the threshold energy of the excitation is given. For all other reactions, the energy released is listed as E_{rel}. Per Capitelli et al. [50], vibrational relaxation is assumed to occur stepwise through the reaction:

$$N_2(v) + M \rightarrow^{k^M_{v,v-1}} N_2(v-1) + M + 0.29 \text{ eV} \tag{B.1}$$

Where, assuming no anharmonicity,

$$k^M_{v,v-1} = v k^M_{1,0} \tag{B.2}$$

The rates for the various quenching species are given in Table B.8.

Table B.1
Electron Impact Excitation/Dissociation. *Cross-Section* refers to the name of the reaction in the cross-sections downloaded from the listed reference.

No.	Equation	Cross-Section	Threshold (eV)	Ref
A1	$e + N_2 \rightarrow e + N_2(A)$	$N_2(A3, v0-4)$	6.17	[34]
		$N_2(A3, v5-9)$	7.00	[34]
		$N_2(A3, v10-)$	7.80	[34]
A2	$e + N_2 \rightarrow e + N_2(B)$	$N_2(B3)$	7.35	[34]
		$N_2(W3)$	7.36	[34]
		$N_2(B'3)$	8.16	[34]
A3	$e + N_2 \rightarrow e + N_2(a')$	$N_2(a')$	8.40	[34]
		$N_2(a1)$	8.55	[34]
		$N_2(w1)$	8.89	[34]
A4	$e + N_2 \rightarrow e + N_2(C)$	$N_2(C3)$	11.03	[34]
		$N_2(E3)$	11.89	[34]
A5	$e + N_2 \rightarrow e + N_2$	$N_2(a''1)$	12.25	[34]
		$N_2(SUM)$	13.00	[34]
A6	$e + O_2 \rightarrow e + O + O$	O_2(6.00 eV)	6.00	[37]
		O_2(8.4 eV)	8.40	[37]
		O_2(9.97 eV)	9.97	[37]
A7	$e + CH_4 \rightarrow e + CH_3 + H$	CH_4(7.90 eV)	7.90	[38]
A8–15	$e + N_2 \rightarrow e + N_2(v)$	$N_2(v = 1-8)$	$0.29v$	[34]
A16–19	$e + O_2 \rightarrow e + O_2$	$O_2(v = 1-4)$	$0.19v$	[37]
A20	$e + CH_4 \rightarrow e + CH_4$	CH_4^*(0.159 eV)	0.16	[38]
		CH_4^*(0.37 eV)	0.37	[38]

Table B.2
Electron Impact Ionization.

No.	Equation	Threshold (eV)	Ref
B1	$e + N_2 \rightarrow 2e + N_2^+$	15.60	[34]
B2	$e + O_2 \rightarrow 2e + O_2^+$	12.06	[37]
B3	$e + CH_4 \rightarrow 2e + CH_4^+$	12.90	[38]
B4	$e + H_2O \rightarrow 2e + H_2O^+$	13.76	[38]
B5	$e + CO_2 \rightarrow 2e + CO_2^+$	13.70	[38]

Table B.3
Three Body attachment.

No.	Equation	Rate (cm^6s^{-1})	E_{rel} (eV)	Ref
C1–5	$2e + N_2^+ \rightarrow e + N_2$		15.60	
	$2e + O_2^+ \rightarrow e + O_2$		12.06	
	$2e + H_2O^+ \rightarrow e + H_2O$	$7.0 \times 10^{-20} \left(\frac{300}{T_e}\right)^{4.5}$	12.90	[50] pg 140
	$2e + CO_2^+ \rightarrow e + CO_2$		13.76	
	$2e + CH_4^+ \rightarrow e + CH_4$		13.70	
C6–10	$e + M + N_2^+ \rightarrow M + N_2$		15.60	
	$e + M + O_2^+ \rightarrow M + O_2$		12.06	
	$e + M + H_2O^+ \rightarrow M + H_2O$	$6.0 \times 10^{-27} \left(\frac{300}{T_e}\right)^{1.5}$	12.90	[50] pg 140
	$e + M + CO_2^+ \rightarrow M + CO_2$		13.76	
	$e + M + CH_4^+ \rightarrow M + CH_4$		13.70	

Appendix C. Supplementary data

Supplementary material related to this article can be found online at https://doi.org/10.1016/j.combustflame.2025.114484.

Table B.4
Dissociative Recombination.

No.	Equation	Rate (cm^3s^{-1})	E_{rel} (eV)	Ref
D1	$e + O_2^+ \rightarrow 2O$	$2.0 \times 10^{-7} \left(\frac{300}{T_e}\right)^{1.0}$	6.894	[35] eqn 40
D2	$e + CH_4^+ \rightarrow CH_3 + H$	$0.18 \cdot 1.17^{-6} \left(\frac{300}{T_e}\right)^{0.66}$	8.344	[63]
D3	$e + CH_4^+ \rightarrow CH_2 + 2H$	$0.51 \cdot 1.17^{-6} \left(\frac{300}{T_e}\right)^{0.66}$	3.540	[63]
D4	$e + CH_4^+ \rightarrow CH_2 + H_2$	$0.06 \cdot 1.17^{-6} \left(\frac{300}{T_e}\right)^{0.66}$	8.060	[63]
D5	$e + CH_4^+ \rightarrow CH + H_2 + H$	$0.23 \cdot 1.17^{-6} \left(\frac{300}{T_e}\right)^{0.66}$	3.675	[63]
D6	$e + H_2O^+ \rightarrow OH + H$	$0.20 \cdot 6.3 \times 10^{-7} \left(\frac{300}{T_e}\right)^{0.35}$	8.858	[64]
D7	$e + H_2O^+ \rightarrow O + H_2$	$0.09 \cdot 6.3 \times 10^{-7} \left(\frac{300}{T_e}\right)^{0.35}$	8.670	[64]
D8	$e + H_2O^+ \rightarrow O + 2H$	$0.71 \cdot 6.3 \times 10^{-7} \left(\frac{300}{T_e}\right)^{0.35}$	4.150	[64]
D9	$e + CO_2^+ \rightarrow CO + O$	$6.5 \times 10^{-7} \left(\frac{300}{T_e}\right)^{0.8}$	8.188	[65]

Table B.5
Optical Transitions; any energy released is assumed to radiate out of the system.

No.	Equation	Rate (s^{-1})	Ref
E1	$N_2(B) \rightarrow N_2(A) + h\nu$	1.34×10^5	[50] table 9.1
E2	$N_2(C) \rightarrow N_2(B) + h\nu$	2.45×10^7	[50] table 9.1

Table B.6
Collisional Quenching of N_2 electronically excited states.

No.	Equation	Rate (cm^3s^{-1})	E_{rel} (eV)	Ref
F1	$N_2(A) + O_2 \rightarrow N_2 + 2O$	2.5×10^{-12}	1.004	[35] eqn 100
F2	$N_2(B) + O_2 \rightarrow N_2 + 2O$	3.0×10^{-10}	2.184	[50] table 9.3
F3	$N_2(a') + O_2 \rightarrow N_2 + 2O$	2.8×10^{-11}	3.234	[50] table 9.3
F4	$N_2(C) + O_2 \rightarrow N_2 + 2O$	3.0×10^{-10}	5.864	[50] table 9.3
F5	$N_2(A) + O \rightarrow N_2 + O$	2.1×10^{-11}	6.170	[50] table 9.3
F6	$N_2(A) + N_2 \rightarrow 2N_2$	3.0×10^{-16}	6.170	[50] table 9.3
F7	$N_2(B) + N_2 \rightarrow 2N_2$	2.0×10^{-12}	8.160	[50] table 9.3
F8	$N_2(B) + N_2 \rightarrow N_2(A) + N_2$	3.0×10^{-11}	1.990	[50] table 9.3
F9	$N_2(a') + N_2 \rightarrow N_2(B) + N_2$	1.9×10^{-13}	.240	[50] table 9.3
F10	$N_2(C) + N_2 \rightarrow N_2(a') + N_2$	1.0×10^{-11}	2.630	[50] table 9.3
F11	$N_2(A) + N_2(A) \rightarrow N_2(B) + N_2$	3.0×10^{-10}	4.180	[50] table 9.3
F12	$N_2(A) + N_2(A) \rightarrow N_2(C) + N_2$	1.5×10^{-10}	3.940	[50] table 9.3
F13	$N_2(A) + CH_4 \rightarrow CH_3 + H + N_2$	3.3×10^{-15}	1.614	[49]
F14	$N_2(B) + CH_4 \rightarrow CH_3 + H + N_2$	3.0×10^{-10}	2.794	[66]
F15	$N_2(a') + CH_4 \rightarrow CH_3 + H + N_2$	5.2×10^{-10}	3.844	[67]
F16	$N_2(C) + CH_4 \rightarrow CH_3 + H + N_2$	5.0×10^{-10}	6.474	[49]

Table B.7
Charge Exchange Reactions.

No.	Equation	Rate (cm^3s^{-1})	E_{rel} (eV)	Ref
G1	$N_2^+ + O_2 \rightarrow O_2^+ + N_2$	$6.0 \times 10^{-11} \left(\frac{300}{T_g}\right)^{0.05}$	3.540	[50] pg 179
G2	$N_2^+ + H_2O \rightarrow H_2O^+ + N_2$	2.3×10^{-9}	1.840	[50] pg 179
G3	$H_2O^+ + O_2 \rightarrow O_2^+ + H_2O$	4.3×10^{-10}	1.700	[50] pg 179
G4	$CO_2^+ + O_2 \rightarrow O_2^+ + CO_2$	5.3×10^{-11}	1.640	[68]

Table B.8
Rates for quenching of N_2 vibrational states in Eqs. (B.1) and (B.2).

M	$k_{1,0}^M$ (cm^3s^{-1})	Ref
N_2	$7.8 \times 10^{-12} T_g \exp\left(218 T_g^{-1/3} + 690 T_g^{-1}\right) \left[1 - \exp\left(-\frac{3400}{T_g}\right)\right]^{-1}$	[50] pg 105
H_2O	$2.5 \times 10^{-12} T_g \exp\left(-21.18 T_g^{-1/3}\right)$	[50] pg 105
O	$1.2 \times 10^{-13} \exp\left(-27.6 T_g^{-1/3}\right)$	[50] pg 105
O_2	$k_{1,0}^{N_2}$	assumed by [51]
CH_4	$5.4 \times 10^{-15} T_g \exp\left(-44.5 T_g^{-1/3}\right) \left[1 - \exp\left(\frac{-3400}{T_g}\right)\right]$	[52]

References

[1] Y. Ju, W. Sun, Plasma assisted combustion: Dynamics and chemistry, Prog Energ Combust 48 (2015) 21–83.

[2] A. Starikovskiy, Physics and chemistry of plasma-assisted combustion, Philos T R Soc A 373 (2048) (2015) 20150074.

[3] T. Ombrello, S.H. Won, Y. Ju, S. Williams, Flame propagation enhancement by plasma excitation of oxygen. Part I: Effects of O3, Combust. Flame 157 (10) (2010) 1906–1915.
[4] S.M. Starikovskaia, Plasma assisted ignition and combustion, J Phys D Appl Phys 39 (16) (2006) R265–R299.
[5] I.N. Kosarev, N.L. Aleksandrov, S.V. Kindysheva, S.M. Starikovskaia, A.Y. Starikovskii, Kinetics of ignition of saturated hydrocarbons by nonequilibrium plasma: CH4-containing mixtures, Combust. Flame 154 (3) (2008) 569–586.
[6] S. Barbosa, G. Pilla, D.A. Lacoste, P. Scouflaire, S. Ducruix, C.O. Laux, D. Veynante, Influence of nanosecond repetitively pulsed discharges on the stability of a swirled propane/air burner representative of an aeronautical combustor, Philos T R Soc A 373 (2048) (2015) 20140335.
[7] G. Vignat, N. Minesi, P.R. Soundararajan, D. Durox, A. Renaud, V. Blanchard, C.O. Laux, S. Candel, Improvement of lean blow out performance of spray and premixed swirled flames using nanosecond repetitively pulsed discharges, P Combust Inst 38 (4) (2021) 6559–6566.
[8] I.V. Adamovich, I. Choi, N. Jiang, J.H. Kim, S. Keshav, W.R. Lempert, E. Mintusov, M. Nishihara, M. Samimy, M. Uddi, Plasma assisted ignition and high-speed flow control: Non-thermal and thermal effects, Plasma Sources Sci T 18 (3) (2009) 034018.
[9] J.K. Lefkowitz, M. Uddi, B.C. Windom, G. Lou, Y. Ju, In situ species diagnostics and kinetic study of plasma activated ethylene dissociation and oxidation in a low temperature flow reactor, P Combust Inst 35 (3) (2015) 3505–3512.
[10] D.A. Lacoste, D.A. Xu, J.P. Moeck, C.O. Laux, Dynamic response of a weakly turbulent lean-premixed flame to nanosecond repetitively pulsed discharges, P Combust Inst 34 (2) (2013) 3259–3266.
[11] T. Ombrello, S.H. Won, Y. Ju, S. Williams, Flame propagation enhancement by plasma excitation of oxygen. Part II: Effects of O2(a1Δg), Combust. Flame 157 (10) (2010) 1916–1928.
[12] A. Elkholy, Y. Shoshyn, S. Nijdam, J.A. van Oijen, E.M. van Veldhuizen, U. Ebert, L.P. de Goey, Burning velocity measurement of lean methane-air flames in a new nanosecond DBD microplasma burner platform, Exp. Therm. Fluid Sci. 95 (January) (2018) 18–26.
[13] C.O. Laux, Applications of plasma discharges to combustion, J. Combust. Soc. Jpn. 64 (209) (2022) 257–264.
[14] G. Pilla, D. Galley, D.A. Lacoste, F. Lacas, D. Veynante, C.O. Laux, Stabilization of a turbulent premixed flame using a nanosecond repetitively pulsed plasma, IEEE T Plasma Sci 34 (6) (2006) 2471–2477.
[15] Q.L.L. Pham, D.A. Lacoste, C.O. Laux, Stabilization of a premixed methane-air flame using nanosecond repetitively pulsed discharges, IEEE T Plasma Sci 39 (11) (2011) 2264–2265.
[16] F. Di Sabatino, D.A. Lacoste, Enhancement of the lean stability and blow-off limits of methane-air swirl flames at elevated pressures by nanosecond repetitively pulsed discharges, J Phys D Appl Phys 53 (35) (2020) 355201.
[17] M. Castela, B. Fiorina, A. Coussement, O. Gicquel, N. Darabiha, C.O. Laux, Modelling the impact of non-equilibrium discharges on reactive mixtures for simulations of plasma-assisted ignition in turbulent flows, Combust. Flame 166 (2016) 133–147.
[18] T.S. Taneja, T. Ombrello, J. Lefkowitz, S. Yang, Large eddy simulation of plasma assisted ignition: Effects of pulse repetition frequency, number of pulses, and pulse energy, Combust. Flame 267 (2024) 113574.
[19] N. Barleon, D. Lacoste, A. Alkhalifa, O. Vermorel, B. Cuenot, Numerical investigation of lean methane flame response to nrp discharges actuation, Combust. Flame 270 (2024) 113745.
[20] X. Mao, H. Zhong, Y. Ju, 2D modeling of plasma-assisted H2/Air ignition in a nanosecond discharge with detailed chemistry, AIAA Scitech 2021 Forum (January) (2021) 1–6.
[21] X. Mao, Q. Chen, A.C. Rousso, T.Y. Chen, Y. Ju, Effects of controlled non-equilibrium excitation on H2/O2/He ignition using a hybrid repetitive nanosecond and DC discharge, Combust. Flame 206 (2019) 522–535.
[22] T.S. Taneja, P.N. Johnson, S. Yang, Nanosecond pulsed plasma assisted combustion of ammonia-air mixtures: Effects on ignition delays and NOx emission, Combust. Flame 245 (2022) 1–18.
[23] G.P. Smith, D.M. Golden, M. Frenklach, N.W. Moriarty, B. Eiteneer, M. Goldenberg, C.T. Bowman, R.K. Hanson, S. Song, J. William C. Gardiner, V.V. Lissianski, Z. Qin, GRI-Mech 3.0 http://combustion.berkeley.edu/gri-mech/version30/text30.html.
[24] H. Wang, X. You, A.V. Joshi, S.G. Davis, A. Laskin, F. Egolfopoulos, C.K. Law, USc mech version II. High-temperature combustion reaction model of $H2/CO/C1-C4$ compounds, 2007, http://ignis.usc.edu/USC_Mech_II.htm.
[25] A. Reuther, J. Kepner, C. Byun, S. Samsi, W. Arcand, D. Bestor, B. Bergeron, V. Gadepally, M. Houle, M. Hubbell, M. Jones, A. Klein, L. Milechin, J. Mullen, A. Prout, A. Rosa, C. Yee, P. Michaleas, Interactive supercomputing on 40,000 cores for machine learning and data analysis, in: 2018 IEEE High Performance Extreme Computing Conference, HPEC, IEEE, 2018, pp. 1–6.
[26] S. Pancheshnyi, B. Eismann, G. Hagelaar, L. Pitchford, Computer code ZDPlasKin, http://www.zdplaskin.laplace.univ-tlse.fr (University of Toulouse, LAPLACE, CNRS-UPS-INP, Toulouse, France, 2008).
[27] G.J.M. Hagelaar, L.C. Pitchford, Solving the Boltzmann equation to obtain electron transport coefficients and rate coefficients for fluid models, Plasma Sources Sci T 14 (4) (2005) 722–733.
[28] D.G. Goodwin, H.K. Moffat, R.L. Speth, Cantera: An object-oriented software toolkit for chemical kinetics, thermodynamics, and transport processes. , 2016, http://dx.doi.org/10.5281/zenodo.1174508, http://www.cantera.org.
[29] X. Mao, A. Rousso, Q. Chen, Y. Ju, Numerical modeling of ignition enhancement of CH 4 /o 2 /he mixtures using a hybrid repetitive nanosecond and DC discharge, P Combust Inst 37 (4) (2019) 5545–5552.
[30] S. MacNamara, G. Strang, Operator splitting, in: R. Glowinski, S.J. Osher, W. Yin (Eds.), Splitting Methods in Communication, Imaging, Science, and Engineering, Springer International Publishing. Switzerland, 2016, pp. 95–114.
[31] C.A. Pavan, Nanosecond Pulsed Plasmas in Dynamic Combustion Environments (Ph.D. thesis), Massachusetts Institute of Technology, 2023.
[32] A. Burcat, Thermochemical data for combustion calculations, in: W.C. Gardiner Jr. (Ed.), Combustion Chemistry, Springer, NY, 1984, pp. 455–473.
[33] S. Pancheshnyi, S. Biagi, M. Bordage, G. Hagelaar, W. Morgan, A. Phelps, L. Pitchford, The lxcat project: Electron scattering cross sections and swarm parameters for low temperature plasma modeling, Chem. Phys. 398 (1) (2012) 148–153.
[34] A.V. Phelps, L.C. Pitchford, SIGLO database. , in: Phys. Rev. a, vol. 31, 1985, p. 2932, http://www.lxcat.laplace.univ-tlse.fr.
[35] I.A. Kossyi, A.Y. Kostinsky, A.A. Matveyev, V.P. Silakov, Kinetic scheme of the non-equilibrium discharge in nitrogen-oxygen mixtures, Plasma Sources Sci T 1 (3) (1992) 207–220.
[36] A. Kazakov, M. Frenklach, DRM19 Mechanism. http://combustion.berkeley.edu/drm/.
[37] P. Lawton, PHELPS database, 69, 2013, p. 1055, http://www.lxcat.laplace.univ-tlse.fr.
[38] M. Hayashi, Hayashi database. www.lxcat.net/Hayashi. URL www.lxcat.net/Hayashi.
[39] N. Aleksandrov, E. Bazelyan, A. Ponomarev, A.Y. Starikovsky, Kinetics of charged species in non-equilibrium plasma in water vapor- and hydrocarbon-containing gaseous mixtures, J Phys D Appl Phys 55 (38) (2022) 383002.
[40] N.A. Popov, S.M. Starikovskaia, Relaxation of electronic excitation in nitrogen/oxygen and fuel/air mixtures: fast gas heating in plasma-assisted ignition and flame stabilization, Prog. Energ. Combust 91 (2022) 1–78.
[41] R.J. Dijoud, N. Laws, C. Guerra-Garcia, Mapping the performance envelope and energy pathways of plasma-assisted ignition across combustion environments, Combust. Flame 271 (2025) 113793.
[42] S. Nagaraja, V. Yang, Z. Yin, I. Adamovich, Ignition of hydrogen-air mixtures using pulsed nanosecond dielectric barrier plasma discharges in plane-to-plane geometry, Combust. Flame 161 (4) (2014) 1026–1037.
[43] I.V. Adamovich, M. Nishihara, I. Choi, M. Uddi, W.R. Lempert, Energy coupling to the plasma in repetitive nanosecond pulse discharges, Phys. Plasmas 16 (11) (2009) 113505.
[44] A.C. Rousso, B.M. Goldberg, T.Y. Chen, S. Wu, A. Dogariu, R.B. Miles, E. Kolemen, Y. Ju, Time and space resolved diagnostics for plasma thermal-chemical instability of fuel oxidation in nanosecond plasma discharges, Plasma Sources Sci T 29 (10) (2020).
[45] I.N. Kosarev, N.L. Aleksandrov, S.V. Kindysheva, S.M. Starikovskaia, A.Y. Starikovskii, Kinetics of ignition of saturated hydrocarbons by nonequilibrium plasma: C2h6- to C5h12-containing mixtures, Combust. Flame 156 (1) (2009) 221–233.
[46] S.M. Starikovskaia, K. Allegraud, O. Guaitella, A. Rousseau, On electric field measurements in surface dielectric barrier discharge, J Phys D Appl Phys 43 (12) (2010) 124007.
[47] J.K. Lefkowitz, P. Guo, A. Rousso, Y. Ju, Species and temperature measurements of methane oxidation in a nanosecond repetitively pulsed discharge, Philos T R Soc A 373 (2048) (2015).
[48] C.A. Pavan, C. Guerra-Garcia, Nanosecond pulsed discharge dynamics during passage of a transient laminar flame, Plasma Sources Sci T 31 (11) (2022) 115016.
[49] M.S. Bak, H. Do, M.G. Mungal, M.A. Cappelli, Plasma-assisted stabilization of laminar premixed methane/air flames around the lean flammability limit, Combust. Flame 159 (10) (2012) 3128–3137.
[50] M. Capitelli, C.M. Ferreira, F. Gordiets, A.I. Osipov, Plasma Kinetics in Atmospheric Gases, first ed., Springer-Verlag Berlin Heidelberg, New York, NY, 2000.
[51] A. Starikovskiy, N. Aleksandrov, Plasma-assisted ignition and combustion, Prog Energ Combust 39 (1) (2013) 61–110.
[52] N.A. Popov, Fast gas heating in a nitrogen-oxygen discharge plasma: I. Kinetic mechanism, J Phys D Appl Phys 44 (28) (2011).
[53] C. Guerra-Garcia, C.A. Pavan, The backward problem in plasma-assisted combustion: Experiments of nanosecond pulsed discharges driven by flames, Appl. Energy Combust. Sci. 15 (March) (2023) 100155.
[54] C.A. Pavan, C. Guerra-Garcia, Modeling flame speed modification by nanosecond pulsed discharges to inform experimental design, in: AIAA SCITECH 2023 Forum, (January) American Institute of Aeronautics and Astronautics, Reston, Virginia, 2023, pp. 1–15.
[55] T. Bergman, A. Lavine, F. Incropera, D. Dewitt, Fundamentals of Heat and Mass Transfer, Seventh ed., John Wiley & Sons, Inc, 2011.
[56] D. Givoli, Non-reflecting boundary conditions, J. Comput. Phys. 94 (1) (1991) 1–29.

[57] R.J. Kee, J.F. Grcar, M.D. Smooke, J.A. Miller, E. Meeks, PREMIX:A FORTRAN Program for Modeling Steady Laminar One-Dimensional Premixed Flames, Tech. rep., 195.

[58] R. Löhner, An adaptive finite element scheme for transient problems in CFD, Comput. Method Appl M 61 (3) (1987) 323–338.

[59] B. Fryxell, K. Olson, P. Ricker, F.X. Timmes, M. Zingale, D.Q. Lamb, P. MacNeice, R. Rosner, J.W. Truran, H. Tufo, FLASH: An adaptive mesh hydrodynamics code for modeling astrophysical thermonuclear flashes, Astrophys. J Supp S 131 (1) (2000) 273–334.

[60] C.M. Rhie, W.L. Chow, Numerical study of the turbulent flow past an airfoil with trailing edge separation, AIAA J. 21 (11) (1983) 1525–1532.

[61] P. Bartholomew, F. Denner, M.H. Abdol-Azis, A. Marquis, B.G. van Wachem, Unified formulation of the momentum-weighted interpolation for collocated variable arrangements, J. Comput. Phys. 375 (2018) 177–208.

[62] S. Zhang, X. Zhao, S. Bayyuk, Generalized formulations for the rhie–chow interpolation, J. Comput. Phys. 258 (2014) 880–914.

[63] R.D. Thomas, I. Kashperka, E. Vigren, W.D. Geppert, M. Hamberg, M. Larsson, M. Af Ugglas, V. Zhaunerchyk, Dissociative recombination of CH4+, J Phys Chem A 117 (39) (2013) 9999–10005.

[64] S. Rosén, A. Derkatch, J. Semaniak, A. Neau, A. Al-Khalili, A. Le Padellec, L. Vikor, R. Thomas, H. Danared, M. Af Ugglas, M. Larsson, Recombination of simple molecular ions studied in storage ring: Dissociative recombination of H2O+, Faraday Discuss. 115 (2000) 295–302.

[65] K. Seiersen, A. Al-Khalili, O. Heber, M.J. Jensen, I.B. Nielsen, H.B. Pedersen, C.P. Safvan, L.H. Andersen, Dissociative recombination of the cation and dication of CO2, Phys. Rev. A 68 (2) (2003) 022708.

[66] L.G. Piper, Energy transfer studies on n 2 (x 1 Σ + g , v) and n 2 (b 3 Π g), J. Chem. Phys. 97 (1) (1992) 270–275.

[67] W.J. Marinelli, W.J. Kessler, B.D. Green, W.A.M. Blumberg, Quenching of n 2 (a 1 Π g , v '=0) by n 2 , o 2 , CO, CO 2 , CH 4 , h 2 , and ar, J. Chem. Phys. 90 (4) (1989) 2167–2173.

[68] A.F. Silva, A.S. Morillo-Candás, A. Tejero-del Caz, L.L. Alves, O. Guaitella, V. Guerra, A reaction mechanism for vibrationally-cold low-pressure CO 2 plasmas, Plasma Sources Sci T 29 (12) (2020) 125020.